Research Square

Preprints are preliminary reports that have not undergone peer review.
They should not be considered conclusive, used to inform clinical practice,
or referenced by the media as validated information.

Comparative in silico evaluation of maslinic and oleanolic acids against protein targets involved in glucose and lipid metabolism

Luka Vidović

015150@mf.uns.ac.rs

Faculty of Medicine, University of Novi Sad

Dragana Dekanski

Institute for the Application of Nuclear Energy, University of Belgrade

Jovan Baljak

Clinical Center of Vojvodina

Ljiljana Tomić

Faculty of Pharmacy, University of Bijeljina

Aleksandra Mesarović

Faculty of Pharmacy, University of Bijeljina

Đorđe Baletić

Faculty of Pharmacy, University of Bijeljina

Aleksandra Jovanović

Institute for the Application of Nuclear Energy, University of Belgrade

Andrea Pirković

Institute for the Application of Nuclear Energy, University of Belgrade

Aleksandar Rašković

Faculty of Medicine, University of Novi Sad

Article

Keywords: maslinic acid, oleanolic acid, molecular docking, molecular dynamics, metabolic targets

Posted Date: November 23rd, 2026

DOI: https://doi.org/10.21203/rs.3.rs-11640418/v1

License: This work is licensed under a Creative Commons Attribution 4.0 International License.
Read Full License

Additional Declarations: No competing interests reported.

Comparative *in silico* evaluation of maslinic and oleanolic acids against protein targets involved in glucose and lipid metabolism

Luka Vidović[1,*], Dragana Dekanski[2], Jovan Baljak[1,3], Ljiljana Tomić[4], Aleksandra Mesarović[4], Đorđe Baletić[1,4], Aleksandra Jovanović[2], Andrea Pirković[2], Aleksandar Rašković[1]

[1] Department of Pharmacology and Toxicology, Faculty of Medicine, University of Novi Sad, 21000 Novi Sad, Serbia

[2] Institute for the Application of Nuclear Energy INEP, University of Belgrade, 11080 Belgrade, Serbia

[3] Center for Forensic Medicine, Toxicology and Molecular Genetics, Clinical Center of Vojvodina, 21000 Novi Sad, Serbia

[4] Bijeljina University, Faculty of Pharmacy, Bijeljina, Bosnia and Herzegovina

Author e-mails: Luka Vidović, 015150@mf.uns.ac.rs; Dragana Dekanski, dragana.dekanski@inep.co.rs; Jovan Baljak, jovan.baljak@mf.uns.ac.rs; Ljiljana Tomić, ljiljana.tomic@ubn.rs.ba; Aleksandra Mesarović, aleksandra.mesarovic@ubn.rs.ba; Đorđe Baletić, djordje.baletic@ubn.rs.ba; Aleksandra Jovanović, ajovanovic@inep.co.rs; Andrea Pirković, andrea.pirkovic@inep.co.rs; Aleksandar Rašković, aleksandar.raskovic@mf.uns.ac.rs.

[*]**Correspondence:** Luka Vidović; 015150@mf.uns.ac.rs.

Abstract

Maslinic and oleanolic acids are olive-derived triterpenes with potential metabolic and antidiabetic activity, but their interactions with individual protein targets remain incompletely defined. We compared their predicted binding to 11β-hydroxysteroid dehydrogenase type 1, protein tyrosine phosphatase 1B, peroxisome proliferator-activated receptor α, and farnesoid X receptor using molecular docking and triplicate molecular dynamics. Reference-ligand and control systems were included, yielding 48 independent 100 ns trajectories and 4.8 μs of aggregate sampling. Both candidates retained contacts with the targeted pockets in all replicas. Farnesoid X receptor and proximal site B of protein tyrosine phosphatase 1B showed comparatively reproducible association, whereas peroxisome proliferator-activated receptor α displayed greater pose heterogeneity. Maslinic acid maintained a conserved Ser170 anchor in 11β-hydroxysteroid dehydrogenase type 1, while oleanolic acid depended more strongly on cofactor contacts. Residue-resolved fluctuations revealed local and terminal variability obscured by whole-protein averages. Molecular mechanics/Poisson–Boltzmann surface area scores did not establish a reliable affinity ranking between the candidates. Projected free-energy landscapes revealed replica-dependent conformational populations. The results support target-specific binding hypotheses and show how persistent local interactions coexist with heterogeneous protein conformations. These findings prioritise target-specific functional assays and pose validation without establishing inhibition, agonism, or antidiabetic efficacy.

Keywords: maslinic acid; oleanolic acid; molecular docking; molecular dynamics; metabolic targets

Introduction

Type 2 diabetes mellitus (T2DM) is associated with disturbances in glucose and lipid metabolism and increased cardiovascular risk. An individual-participant analysis of 102 prospective studies found approximately twofold higher risks of coronary heart disease and ischaemic stroke in people with diabetes after adjustment for conventional risk factors [1]. Current treatment recommendations therefore consider glycaemic control together with cardiovascular, kidney, and weight-related outcomes [2]. The antidiabetic drugs empagliflozin and liraglutide reduced cardiovascular events in patients with T2DM at high cardiovascular risk [3, 4], while tirzepatide produced greater reductions in glycated haemoglobin and body weight than semaglutide 1 mg in the SURPASS-2 clinical trial [5]. These findings have encouraged investigation of complementary pathways involved in this metabolic disease.

Olive-derived compounds have attracted interest in this context. The revised PREDIMED analysis associated Mediterranean diets supplemented with extra-virgin olive oil or nuts with fewer major cardiovascular events than a reduced-fat control diet [6]. A randomised crossover trial also found improved insulin sensitivity and pancreatic β-cell responsiveness after supplementation with an olive-leaf preparation containing oleuropein and hydroxytyrosol [7]. Although these studies evaluated dietary patterns or mixtures rather than individual triterpenes, they provide a clinical context for investigating olive constituents.

Maslinic acid (MAS) and oleanolic acid (OLE) are pentacyclic triterpenoid acids found in olive fruit and leaves [8]. They share the same scaffold, with MAS containing an additional hydroxyl group. In a previous study, our research group quantified both triterpenes in olive leaf extract and found that their retention in liposomal formulations depended on phospholipid composition, with the highest retention in liposomes prepared from hydrogenated phospholipids [9]. In the PREDIABOLE trial, fewer new cases of T2DM occurred in participants with prediabetes who received OLE-enriched olive oil than in those who received the same unenriched oil [10]. The molecular targets underlying this formulation-level effect remain unresolved, and the result does not establish equivalent activity for MAS.

In this study, we selected four proteins involved in glucose and lipid metabolism. 11β-Hydroxysteroid dehydrogenase type 1 (HSD11B1) converts cortisone to cortisol; its selective inhibitor INCB13739 improved glycaemic measures when added to metformin [11]. Protein tyrosine phosphatase 1B (PTP1B) regulates insulin signalling and has been investigated clinically using antisense inhibition [12]. Peroxisome proliferator-activated receptor α (PPARα) regulates hepatic fatty-acid oxidation and the response to fasting, as shown in PPARα-deficient mice [13]. Farnesoid X receptor (FXR) links bile-acid signalling with glucose and lipid metabolism. In a six-week trial in patients with T2DM and fatty liver disease, the FXR agonist obeticholic acid increased insulin sensitivity and altered bile-acid-related measures, while also increasing LDL cholesterol [14].

Two triterpenoid acids (MAS and OLE) were evaluated against HSD11B1, PTP1B, PPARα, and FXR using molecular docking and three 100 ns molecular dynamics (MD) simulations per system, with receptor-specific reference ligands and controls. We examined pose retention, local interactions, and protein conformational variability to identify target-specific binding patterns associated with the additional hydroxyl group in MAS. Residue fluctuations, principal component analysis (PCA), projected free-energy landscapes, and molecular mechanics/Poisson–Boltzmann surface area (MM/PBSA) scores were assessed across individual trajectories.

Results

Docking and reference-pose recovery

Seventeen docking campaigns generated 17,000 search results. Each target had separate native-reference, prepared-reference, MAS, and OLE campaigns; an additional campaign supplied the HSD11B1 cofactor's pose. The reference ligands were cilofexor (CIL), carbenoxolone (CBO), BMS-631707 (REW), and the co-crystallized sulfamic-acid PTP1B inhibitor (Protein Data Bank [PDB] component code UN5) for FXR, HSD11B1, PPARα, and PTP1B, respectively. The selected production poses and their scores are summarised in Table 1 and Supplementary Table S2a. The selected prepared-reference poses had original global docking-score ranks of 1 for CIL, 6 for CBO, 10 for REW, and 1 for UN5, with crystal-reference heavy-atom root-mean-square deviations (RMSDs) of 1.602, 1.154, 1.065, and 0.865 Å, respectively. For CBO, the top-scoring pose was −13.68 kcal mol^{-1} with a crystal-reference RMSD of 1.822 Å, compared with −13.53 kcal mol^{-1} and 1.154 Å for the selected pose. For REW, the corresponding top-scoring and selected poses were −11.63 and −10.99 kcal mol^{-1}, with RMSDs of 3.987 and 1.065 Å (Supplementary Table S2e). The CBO and REW poses were selected for MD because they agreed more closely with the native crystallographic poses, despite ranking below the top-scoring solutions.

OLE scored more favourably than MAS for FXR, HSD11B1, and PPARα, whereas MAS yielded better scores for PTP1B. All reference compounds had more favourable selected-pose scores than the corresponding triterpenes. Alternative docking clusters remained relevant: the selected FXR/OLE cluster contained 27.7% of searches and scored −12.41 kcal mol^{-1}, while a second cluster contained 70.9% and scored −12.07 kcal mol^{-1}. Three MD replicas were initiated from the same selected pose within each ligand–target pair. The three replicas therefore sampled each complex from a common binding configuration.

Ligand retention and local interactions

All 48 production trajectories reached 100 ns with distinct initial velocity seeds and no recorded fatal or LINCS warnings. Both candidates retained contacts with the targeted pocket regions in all replicas. Protein-fitted ligand RMSD nevertheless revealed substantial target-dependent reorientation (Fig. 1). Mean values and between-replica standard deviations are reported in Table

2; individual results for the full trajectory and two sensitivity windows are retained in Supplementary Tables S4b, S5b, S6b, and S7b. All replicas were included in the analysis.

FXR supported comparatively reproducible poses. MAS and OLE ligand RMSDs were 0.210 ± 0.042 and 0.192 ± 0.013 nm, respectively, compared with 0.217 ± 0.014 nm for CIL. Contacts with Met265, Met290, His294, Met328, Ser332, and His447 placed both candidates within the ligand-binding region. MAS formed more geometric protein hydrogen bonds on average than OLE, but its additional polar interactions varied between trajectories. His294 acceptor occupancies were 75.5%, 93.0%, and 63.4% for MAS and 79.0%, 78.4%, and 94.7% for OLE (Fig. 2; Supplementary Table S10a). The MAS–His447 donor interaction occupied 82.5%, 1.6% and 69.1% of frames in replicas 1, 2 and 3, respectively. Thus, pocket retention was accompanied by variability in the polar contacts.

HSD11B1 retained both candidates but showed different anchoring modes. MAS ligand RMSDs were 0.119, 0.166, and 0.427 nm. Despite the third replica's displacement, the Ser170 acceptor interaction occupied 90.99%, 99.01%, and 99.92% of frames. The third replica exchanged predominantly Ala172-associated anchoring for Tyr183 engagement. OLE formed few direct protein hydrogen bonds, averaging 0.04 ± 0.06, but donated a hydrogen bond to the oxidized nicotinamide adenine dinucleotide phosphate cofactor ($NADP^+$; residue code NAP) in 69.27%, 99.86%, and 99.44% of frames. In its first replica, this cofactor interaction was largely lost after 70 ns while pocket contacts persisted. The protein hydrogen-bond count was calculated excluding the cofactor.

PPARα showed greater pose heterogeneity. MAS ligand RMSDs were 0.500, 0.205, and 0.216 nm, while OLE values were 0.536, 0.201, and 0.353 nm. During 50–100 ns, the respective values remained 0.532, 0.236, and 0.227 nm for MAS and 0.609, 0.178, and 0.430 nm for OLE. Persistent Phe273, Gln277, and neighbouring contacts supported intrapocket reorientation. Polar interactions differed sharply among replicas: MAS–His440 acceptor occupancies were 2.8%, 19.7%, and 99.6%, while OLE–Ser280 occupancies were 0.5%, 0.1%, and 98.0%. The replicas therefore sampled distinct polar interaction patterns.

PTP1B supported association with proximal secondary aryl-phosphate site B near Arg24 and Arg254. The candidates' starting poses lay approximately 10.5 Å from Cys215 and Arg221; UN5 also reached the catalytic region. MAS and OLE ligand RMSDs were 0.280 ± 0.013 and 0.305 ± 0.016 nm, respectively. Their late-window site-B contact occupancies were 100% for all MAS replicas and 99.86%, 99.98%, and 100% for OLE. No contacts were detected with the monitored distal allosteric residue set. This observation is conditional on the focused docking grid and the initial site-B poses; it does not establish preference for site B over alternative binding sites. MAS retained Arg24 acceptor interactions in 99.90%, 98.45%, and 99.67% of frames, compared with 71.97%, 97.43%, and 99.87% for OLE. OLE replica 1 rearranged during approximately 60–90 ns, weakening its original Arg24/Arg254 interactions while gaining other contacts.

Residue fluctuations and terminal motion

Backbone root-mean-square fluctuation (RMSF) profiles showed localised changes and substantial replica dependence (Fig. 3 and Supplementary Fig. S4). The modelled HSD11B1 C-terminus contributed pronounced fluctuations. In OLE replica 2, whole-backbone RMSD averaged 0.465 nm. After fitting crystal-supported Cα residues 26–268, core and tail Cα RMSDs were 0.265 and 1.716 nm, respectively (Supplementary Table S11). The larger whole-protein deviation was therefore associated with terminal motion.

Whole-protein mean RMSF also concealed regional differences. PTP1B/OLE and control PTP1B had almost identical means, both approximately 0.0739 nm. In a post hoc descriptive comparison of residues 113–118, however, OLE averaged 0.1590 ± 0.1113 nm and the control system 0.0893 ± 0.0039 nm. The OLE difference was dominated by replica 3; its regional mean was 0.2875 nm, compared with 0.0955 and 0.0940 nm in replicas 1 and 2, respectively. Whole-protein RMSF averages are provided as secondary descriptors in Supplementary Table S12b.

Protein backbone RMSD, radius of gyration, and solvent exposure were broadly compatible with retained compact domains but did not show uniform ligand-induced rigidification or compaction (Supplementary Fig. S2 and Tables S4a, S5a, S6a, and S7a).

Principal components and projected free-energy landscapes

PCA and the corresponding projected free-energy landscapes distinguished local pocket retention from agreement between whole-protein conformational populations (Fig. 4 and Supplementary Fig. S3). The first two principal components accounted for 24.91%, 43.43%, 26.44%, and 17.37% of the combined Cα variance in FXR, HSD11B1, PPARα, and PTP1B, respectively. All systems within a receptor shared the same projection axes and evaluation limits. The Gaussian kernel density estimates describe the sampled PC1–PC2 distributions; lower landscape values identify regions with higher estimated density, with each map independently referenced to its maximum evaluated density. Supplementary Fig. S10 shows the variance spectra.

FXR/MAS and FXR/OLE showed distinct populated regions despite their comparatively reproducible ligand RMSDs. The individual maps identified a displaced second MAS replica and a displaced third OLE replica, whereas the other two replicas in each system occupied more similar regions. PTP1B/OLE showed greater overlap among its three projected distributions than PTP1B/MAS. Thus, the local rearrangement of OLE in PTP1B replica 1 did not imply a correspondingly separated whole-protein PC1/PC2 population. Local ligand rearrangement and whole-protein conformational separation did not follow the same pattern.

HSD11B1/OLE displayed distinct replica populations, including the separated second replica. The modelled C-terminal segment, residues 269–284, accounted for 63.24% and 70.25% of the squared PC1 and PC2 vector norms, respectively. These percentages describe the spatial composition of the two modes, rather than their explained-variance fractions. The HSD11B1 landscapes therefore substantially reflect terminal motion. PPARα/OLE also showed separated

populations, consistent with the nonuniform configurations observed across its trajectories. Reference-ligand, control, and individual-replica landscapes are presented in Supplementary Figs. S5–S9; construction settings and descriptive summaries are provided in Supplementary Tables S13a–d and S14a–b. The individual-replica maps and unsmoothed projections showed which populations contributed to each pooled distribution.

MM/PBSA endpoint scores

Molecular mechanics/Poisson–Boltzmann surface area (MM/PBSA) scores are reported in Table 2 and Supplementary Fig. S1. For FXR, the MAS–OLE difference was only 0.97 kcal mol^{-1} over 0–100 ns and decreased to 0.29 kcal mol^{-1} over 50–100 ns. PPARα and PTP1B likewise showed small separations relative to replica variability and model uncertainty. HSD11B1 showed a consistent descriptive order of CBO, MAS, and OLE, with full-window scores of −61.23 ± 3.08, −54.96 ± 2.96, and −48.76 ± 0.90 kcal mol^{-1}. The late-window values retained this order but showed increased dispersion, especially for OLE.

More favourable endpoint scores did not necessarily accompany better preservation of a starting pose. PTP1B/OLE replica 1 became more favourable during its late reorganisation despite weakening original polar contacts. The endpoint scores therefore did not consistently track preservation of the initial polar contacts.

Discussion

The olive-derived triterpenoid acids MAS and OLE remained associated with the targeted pockets throughout the triplicate simulations, but their poses and polar interactions differed among receptors. Farnesoid X receptor and proximal PTP1B site B showed comparatively reproducible local associations. PPARα accommodated more heterogeneous poses, whereas HSD11B1 showed persistent direct protein anchoring for MAS and greater cofactor involvement for OLE. All simulations began from prebound configurations, so these results describe the persistence and rearrangement of the selected complexes.

The results obtained for FXR are consistent with functional evidence for OLE. Wang et al. reported inhibition of chenodeoxycholic acid (CDCA)-induced FXR transactivation by parent OLE, with an IC_{50} of 13.69 μM [15]. Our simulations support a persistent OLE–FXR complex but do not distinguish antagonism from other functional responses or validate the predicted pose. MAS also remained in the pocket and formed more protein hydrogen bonds on average, although its polar contacts varied among replicas. These differences did not establish a consistent affinity advantage for either compound.

Both triterpenes have direct experimental support as PTP1B inhibitors. Ponce-Zea et al. reported IC_{50} values of 1.7 ± 0.8 μM for OLE and 1.28 ± 0.1 μM for MAS, expressed as mean ± standard error of the mean (SEM) from triplicate experiments. MAS showed noncompetitive inhibition, with a K_i of 3.2 ± 0.6 μM; the inhibition mechanism of OLE was not determined [16]. Their docking analysis used the distal allosteric pocket in PDB structure 1T49. In contrast, the

predicted binding modes in the present study occupied the proximal secondary aryl-phosphate site, where Arg24 and Arg254 contribute to ligand recognition [17]. The persistent MAS–Arg24 interaction therefore supports an alternative binding-site hypothesis. Noncompetitive kinetics do not resolve which site is occupied, and site-directed experiments will be needed to distinguish these models.

OLE enhanced human PPARα reporter activity in HEK293 cells at 100–300 μM, and MK-886 suppressed this response [18]. The animal experiments in that study used total pomegranate flower extract, so the physiological findings cannot be assigned to purified OLE. For MAS, a mouse study reported increased hepatic PPARα expression alongside docking and MD predictions, but high-dose treatment also promoted gallstone formation and cholestatic liver injury [19]. Neither expression changes nor computational predictions establish direct receptor agonism. PPARα crystal structures identify a polar interaction network involving Ser280, Tyr314, His440, and Tyr464 [20]. Our MAS and OLE complexes contacted this region but differed among replicas, without consistently maintaining a single activation-associated network. The simulations therefore support PPARα binding hypotheses while leaving the direction and magnitude of a transcriptional response unresolved.

HSD11B1 has less direct parent-compound evidence in the literature examined here. A study of oleanan and ursan derivatives demonstrated inhibition of the human enzyme and a strong dependence on chemical substitution [21]. In our simulations, MAS maintained a Ser170 interaction in all replicas and had more favourable MM/PBSA scores than OLE. OLE occupied a distinct configuration with frequent cofactor contacts. These observations support direct enzyme assays of both compounds, with the MAS–Ser170 interaction providing a specific structural hypothesis.

Independent velocity initialisation revealed substantial differences among trajectories, including PPARα pose heterogeneity, displacement of HSD11B1/MAS in one replica, and rearrangement of PTP1B/OLE in another. This agrees with previous work showing that conclusions from single MD trajectories may be poorly reproducible [22]. The three replicas in each system shared one docking pose, however, and do not exhaust the possible binding configurations. Crystallographic agreement guided selection of the CBO and REW starting poses, which retained original docking-score ranks of 6 and 10, respectively. The simulations consequently assess the selected complexes rather than validating docking-score ranking across all poses.

Protein motion also depended on the structural models. The modelled HSD11B1 C-terminus contributed strongly to whole-protein RMSD and the leading principal components, whereas residue-level and core analyses separated these motions from the more stable protein region. FXR and PTP1B retained crystallographic Ramachandran outliers, while the steric overlap in FXR identified during preparation was absent from the examined production contacts. These features were considered alongside interaction and conformational analyses.

The MM/PBSA scores and projected landscapes describe different aspects of the sampled complexes. Endpoint scores depended on the molecular model and sampled configurations and did not provide a reliable general MAS–OLE affinity ranking. PC1 and PC2 represented only part of the protein variance, and several systems showed substantial differences between replica populations. Low-dimensional landscapes can omit conformational features relevant to folding dynamics [23]. In our maps, smoothing and equal-weight pooling summarised the sampled distributions but did not establish transitions between separated regions or equilibrium free-energy differences. The results remain conditional on the fixed protonation states, reconstructed regions, and selected starting poses.

Overall, FXR and PTP1B provide the clearest targets for experimental testing of the local interactions predicted here. PPARα remains plausible but showed greater pose heterogeneity, and HSD11B1 requires direct parent-compound inhibition measurements. The simulations identify testable binding configurations rather than a consistent affinity ranking between MAS and OLE. Matched binding and functional assays are needed to determine whether these configurations produce inhibition, agonism, or other receptor responses.

Methods

Protein structures and preparation

Protein structures were obtained from chain A of PDB entries 7VUE for FXR, 2BEL for HSD11B1, 2REW for PPARα, and 2F6Z for PTP1B. The reference ligands were cilofexor (crystal code 811, simulation label CIL), carbenoxolone (CBO), BMS-631707 (REW), and UN5, respectively. Missing heavy atoms were repaired, and fixed protonation states were assigned for pH 7.4 with PROPKA [24]. Residue states were encoded in force-field residue names before GROMACS regenerated compatible hydrogens and termini. Protonation states remained fixed throughout the simulations.

Missing regions of HSD11B1, PPARα, and PTP1B were modelled with MODELLER [25]. Ten candidates were generated per modelling strategy, assessed for stereochemistry, template agreement, and environmental contacts, and ranked with consideration of DOPE. Constructs comprised FXR residues 245–470, HSD11B1 residues 26–284, PPARα residues 196–468, and PTP1B residues 1–298. MolProbity/CCTBX checks assessed local geometry and clashes. Oxidised nicotinamide adenine dinucleotide phosphate ($NADP^+$; PDB residue code NAP) was retained in every HSD11B1 system, including the control; its prepared pose was obtained by docking. Receptor constructs and residue numbering, ligand/cofactor formal charges and molecular topology details, and prepared protein stereochemical summaries are detailed in Supplementary Tables S1a and S3a–b. PTP1B Cys215 was represented as neutral CYS. Control systems contained no MAS, OLE or receptor-specific reference ligand. The HSD11B1 control retained NAP.

Ligand preparation and parameterisation

Structures were standardised while preserving specified stereochemistry. Ionisation states were enumerated with Dimorphite-DL at pH 7.4 ± 1.0 [26], and RDKit was used for tautomer and conformer generation. For MAS and OLE, 20 RDKit conformers were requested with seed 20260719, screened with GFN2-xTB [27] using ALPB water and loose optimisation criteria, subjected to CREST quick conformational sampling [28], and optimised with tight GFN2-xTB criteria. We used xTB 6.7.1 and CREST 3.0.2. MAS and OLE were represented as carboxylates with net charge −1. CIL, CBO, and UN5 had net charges of −1, −2, and −2, respectively. REW contained a protonated β-lactam nitrogen and a carboxylate, giving a net charge of 0. NAP contained N7-protonated adenine and had a net charge of −2. CBO and UN5 received xTB screening without CREST. CIL, REW and NAP preparation used neither xTB nor CREST.

Geometries were optimised with ORCA [29], version 6.1.1, using gas-phase restricted Hartree–Fock/6-31G* with TightSCF and TightOpt. Charges were fitted with ORCA's native restrained electrostatic potential (RESP) procedure on a CHELPG-derived grid, using hyperbolic-restraint parameters a = 0.0005 and b = 0.1. Docking-input heavy-atom geometries matched the resulting optimised structure data file (SDF) structures. Selected docked coordinates were mapped onto chemically defined ligand structures before parameter assignment with the second-generation general Amber force field (GAFF2) with Antechamber and parmchk2. GAFF2 belongs to the general Amber force-field framework [30]. LEaP assembled the Amber topologies, and ParmEd exported GROMACS files while retaining the ORCA charge set. Small rounding corrections restored integer molecular charges. Atom mapping and charge sums were checked for all 13 ligand/cofactor representations.

Molecular docking

Site-focused grids were generated with AutoGrid4, and docking used AutoDock-GPU v1.6-release [31, 32]. Production receptor PDBQT records were generated with Meeko and Gasteiger-based charges and were identical across the candidate and prepared-reference campaigns within each target. HSD11B1 additionally included docked NAP. Polar hydrogens were retained, and nonpolar hydrogens were merged in the united-atom docking representation. Docking charges were distinct from the RESP-derived MD charges.

Grid spacing was 0.375 Å, with side lengths of 25.5, 22.5, 24.0, and 22.5 Å for FXR, HSD11B1, PPARα, and PTP1B. Centres are given in Supplementary Table S2c. Each campaign requested 1,000 searches, population size of 500, random seed of 111, at most 50,000 generations, and 25,000,000 energy evaluations, with heuristics and automatic stopping enabled. ADADELTA provided local optimisation, and poses were clustered at 2 Å with symmetry handling. Native-reference and prepared-production campaigns were analysed separately because their preparations differed. Prepared-reference poses were compared with the native crystallographic heavy-atom coordinates using an ordered atom correspondence and no ligand superposition. For CBO and REW, closer crystallographic agreement determined selection of the MD starting

poses, which had original global docking-score ranks of 6 and 10, respectively. CIL and UN5 used the rank-1 poses. These ranks refer to the original score ordering of the 1,000 search results within each prepared-reference campaign. The selected docking poses were used for topology construction and MD. MAS and OLE were selected from the lowest-scoring solutions at the reported two-decimal precision. For HSD11B1/MAS, HSD11B1/OLE, and PTP1B/MAS, the selected exports occupy the second position in the original output ordering and share the first-listed score. Output order is retained separately from score ties in Supplementary Table S2a. Selected-versus-top-ranked comparisons are given in Supplementary Table S2e. One pose per ligand–target pair initialised the three MD replicas.

Molecular dynamics

Production calculations used GROMACS 2025.4-dev-20251121-560f2601a7, AMBER99SB-ILDN proteins, GAFF2 ligands, and TIP3P water [33, 34]. The setup protocol used rhombic dodecahedral boxes with 1.2 nm minimum solute-to-box separation, neutralisation with Na^+ and Cl^-, and 0.15 M added salt. The spc216 coordinate template initialised water positions; the topology specified TIP3P. Minimisation was configured for up to 50,000 steepest-descent steps and a maximum-force stopping threshold of 1,000 kJ mol^{-1} nm^{-1}. Two 250 ps stages at constant particle number, volume and temperature (NVT) were followed by four stages at constant particle number, pressure and temperature (NPT) lasting 250, 500, 500, and 500 ps. Backbone and ligand-heavy-atom restraint coefficients decreased through the stages as listed in Supplementary Table S1b. Production runs were unrestrained.

Each of 16 receptor/system combinations underwent three 100 ns simulations. Distinct Maxwell-distributed velocities were generated during the first NVT stage; the 48 actual seeds and completion checks are given in Supplementary Table S9. Integration used a 2 fs step with LINCS constraints on bonds involving hydrogen, order 4, and one iteration. Particle-mesh Ewald electrostatics used a 1.0 nm real-space cutoff, 0.12 nm nominal Fourier spacing, fourth-order interpolation, and a relative tolerance of 10^{-5}. Van der Waals interactions used a 1.0 nm cutoff with a potential shift and energy/pressure dispersion corrections. Verlet neighbour lists and three-dimensional periodic boundaries were applied.

Velocity-rescaling maintained 310.15 K with separate solute and water/ion coupling groups. The coupling time was 0.1 ps in NVT and 1.0 ps in NPT and production. Isotropic stochastic cell-rescaling maintained 1 bar with a 5 ps coupling time and compressibility 4.5×10^{-5} bar^{-1}. Coordinates were saved every 10 ps. All production runs reached step 50,000,000.

Structural and interaction analysis

Trajectories were corrected for periodic boundaries before structural analysis. Protein-backbone RMSD used backbone fitting; ligand-heavy-atom RMSD used protein fitting without ligand self-fitting. Each replica's minimised structure was its RMSD reference. Per-residue backbone RMSF used the N, Cα, and carbonyl C selection, with the GROMACS mass-weighted fit. Atomic mean-

square fluctuations about aligned mean coordinates were mass-averaged within each residue before taking the square root. Profiles were calculated separately for each trajectory. Whole-protein mean residue RMSF was the unweighted arithmetic mean of those residue values, retained only as a secondary descriptor. Radius of gyration and solvent-accessible surface area were evaluated for the protein.

Contacts required a receptor–ligand heavy-atom separation of at most 0.4 nm; NAP was included in the HSD11B1 receptor contact definition. Geometric protein–ligand hydrogen bonds used GROMACS hbond with a 0.35 nm donor–acceptor cutoff and a 30° acceptor–donor–hydrogen angle cutoff on the original unrotated trajectory with periodic handling. This protein group excluded NAP. ProLIF 2.2.3 with MDAnalysis 2.10.0 classified interactions chemically [35]. Residue identifiers were mapped to original protein numbering. Selected occupancy comparisons in Fig. 2 illustrate the interactions discussed in the text; the complete interaction tables are available in the deposited project data.

Principal component and projected free-energy analysis

Cα coordinates from 0–100 ns at 10 ps intervals were fitted by unweighted least-squares rotation and translation to the reference structure of the first control replica (MDR1) for the corresponding receptor. Each receptor had one common covariance matrix and PCA basis, calculated about a common mean with equal weights for the four systems and their three replicas. An axis-aligned Gaussian product-kernel density estimate (KDE) was calculated from the PC1–PC2 projections. A condition-specific diagonal Scott bandwidth was calculated from the equally weighted pooled coordinate variance and shared by that condition's three replicas. Replica densities were evaluated on a common 200 × 200 mesh spanning the receptor-wide coordinate range with 2% padding, then averaged with equal weights before Boltzmann inversion, $F = -RT \ln(\rho/\rho_{max})$, at 310.15 K, using $R = 0.00831446261815324$ kJ mol^{-1} K^{-1}. Kernel widths, settings, and diagnostic definitions are given in Supplementary Tables S13a–d and S14a–b.

The contribution of the HSD11B1 modelled tail to each principal component was calculated by summing the squared Cartesian eigenvector elements for Cα atoms of residues 269–284 and dividing by the full eigenvector squared norm. This descriptive spatial decomposition was separate from the fraction of total coordinate variance explained by a principal component.

Endpoint estimates and reporting of variability

Single-trajectory MM/PBSA calculations used gmx_MMPBSA 1.6.5 and MMPBSA.py 16.0 with the internal sander PBSA solver [36]. Each liganded replica contributed 1,001 frames at 100 ps spacing over 0–100 ns. Solute and solvent dielectric constants were 4 and 80, with ionic strength 0.15 M and settings PBRadii = 3, radiopt = 0, inp = 1, and fillratio = 4. NAP was included in the HSD11B1 receptor. The reported endpoint score is the sum of the molecular-mechanics and polar and nonpolar solvation contributions: $\Delta E_{MM} + \Delta G_{PB} + \Delta G_{nonpolar}$.

The trajectory was the unit of replication. Summaries are reported as the mean ± sample standard deviation of the three run means (n = 3). Residue-level profiles likewise show the mean and sample standard deviation across the three run-specific RMSFs. Full-production 0–100 ns values are primary; 20–100 ns and 50–100 ns values are sensitivity analyses rather than asserted equilibrium intervals. Correlated frames and different residues were not counted as independent experimental replicates. No hypothesis tests or conversions of scores into affinity or potency were performed. Supplementary Table S15 lists the deposited data and graphs.

Use of artificial intelligence

ChatGPT (OpenAI) was used to assist with language editing and manuscript formatting.

References

1. Emerging Risk Factors Collaboration. Diabetes mellitus, fasting blood glucose concentration, and risk of vascular disease: a collaborative meta-analysis of 102 prospective studies. *Lancet* **375**, 2215–2222 (2010). https://doi.org/10.1016/S0140-6736(10)60484-9

2. American Diabetes Association Professional Practice Committee for Diabetes. 9. Pharmacologic approaches to glycemic treatment: Standards of Care in Diabetes—2026. *Diabetes Care* **49**, S183–S215 (2026). https://doi.org/10.2337/dc26-S009

3. Zinman, B. et al. Empagliflozin, cardiovascular outcomes, and mortality in type 2 diabetes. *N. Engl. J. Med.* **373**, 2117–2128 (2015). https://doi.org/10.1056/NEJMoa1504720

4. Marso, S. P. et al. Liraglutide and cardiovascular outcomes in type 2 diabetes. *N. Engl. J. Med.* **375**, 311–322 (2016). https://doi.org/10.1056/NEJMoa1603827

5. Frías, J. P. et al. Tirzepatide versus semaglutide once weekly in patients with type 2 diabetes. *N. Engl. J. Med.* **385**, 503–515 (2021). https://doi.org/10.1056/NEJMoa2107519

6. Estruch, R. et al. Primary prevention of cardiovascular disease with a Mediterranean diet supplemented with extra-virgin olive oil or nuts. *N. Engl. J. Med.* **378**, e34 (2018). https://doi.org/10.1056/NEJMoa1800389

7. de Bock, M. et al. Olive (*Olea europaea* L.) leaf polyphenols improve insulin sensitivity in middle-aged overweight men: a randomized, placebo-controlled, crossover trial. *PLoS ONE* **8**, e57622 (2013). https://doi.org/10.1371/journal.pone.0057622

8. Guinda, Á., Rada, M., Delgado, T., Gutiérrez-Adánez, P. & Castellano, J. M. Pentacyclic triterpenoids from olive fruit and leaf. *J. Agric. Food Chem.* **58**, 9685–9691 (2010). https://doi.org/10.1021/jf102039t

9. Baljak, J. et al. Valorization of olive leaf extract via tailored liposomal carriers: comparative analysis of physicochemical features, antioxidant capacity, and stability. Pharmaceuticals 18, 1639 (2025). https://doi.org/10.3390/ph18111639

10. Santos-Lozano, J. M. et al. Prevention of type 2 diabetes in prediabetic patients by using functional olive oil enriched in oleanolic acid: the PREDIABOLE study, a randomized controlled trial. *Diabetes Obes. Metab.* **21**, 2526–2534 (2019). https://doi.org/10.1111/dom.13838

11. Rosenstock, J. et al. The 11-β-hydroxysteroid dehydrogenase type 1 inhibitor INCB13739 improves hyperglycemia in patients with type 2 diabetes inadequately controlled by metformin monotherapy. *Diabetes Care* **33**, 1516–1522 (2010). https://doi.org/10.2337/dc09-2315

12. Digenio, A. et al. Antisense inhibition of protein tyrosine phosphatase 1B with IONIS-PTP-1BRx improves insulin sensitivity and reduces weight in overweight patients with type 2 diabetes. *Diabetes Care* **41**, 807–814 (2018). https://doi.org/10.2337/dc17-2132

13. Kersten, S. et al. Peroxisome proliferator-activated receptor α mediates the adaptive response to fasting. *J. Clin. Invest.* **103**, 1489–1498 (1999). https://doi.org/10.1172/JCI6223

14. Mudaliar, S. et al. Efficacy and safety of the farnesoid X receptor agonist obeticholic acid in patients with type 2 diabetes and nonalcoholic fatty liver disease. *Gastroenterology* **145**, 574–582.e1 (2013). https://doi.org/10.1053/j.gastro.2013.05.042

15. Wang, S. R. et al. Discovery of farnesoid X receptor antagonists based on a library of oleanolic acid 3-*O*-esters through diverse substituent design and molecular docking methods. *Molecules* **22**, 690 (2017). https://doi.org/10.3390/molecules22050690

16. Ponce-Zea, J. E. et al. *In vitro* and *in silico* analysis of PTP1B inhibitors from *Cleistocalyx operculatus* leaves and their effect on glucose uptake. *Nutrients* **16**, 2839 (2024). https://doi.org/10.3390/nu16172839

17. Puius, Y. A. et al. Identification of a second aryl phosphate-binding site in protein-tyrosine phosphatase 1B: a paradigm for inhibitor design. *Proc. Natl Acad. Sci. USA* **94**, 13420–13425 (1997). https://doi.org/10.1073/pnas.94.25.13420

18. Huang, T. H. W. et al. Pomegranate flower improves cardiac lipid metabolism in a diabetic rat model: role of lowering circulating lipids. *Br. J. Pharmacol.* **145**, 767–774 (2005). https://doi.org/10.1038/sj.bjp.0706245

19. Feng, S. et al. Exploring the effects of maslinic acid on gallstone formation and liver injury via the PPAR signaling pathway. *Discov. Med.* **37**, 2907–2922 (2025). https://doi.org/10.24976/Discov.Med.202537203.243

20. Capelli, D. et al. Structural basis for PPAR partial or full activation revealed by a novel ligand binding mode. *Sci. Rep.* **6**, 34792 (2016). https://doi.org/10.1038/srep34792

21. Blum, A., Favia, A. D. & Maser, E. 11β-Hydroxysteroid dehydrogenase type 1 inhibitors with oleanan and ursan scaffolds. *Mol. Cell. Endocrinol.* **301**, 132–136 (2009). https://doi.org/10.1016/j.mce.2008.08.028

22. Knapp, B., Ospina, L. & Deane, C. M. Avoiding false positive conclusions in molecular simulation: the importance of replicas. *J. Chem. Theory Comput.* **14**, 6127–6138 (2018). https://doi.org/10.1021/acs.jctc.8b00391

23. Maisuradze, G. G., Liwo, A. & Scheraga, H. A. How adequate are one- and two-dimensional free energy landscapes for protein folding dynamics? *Phys. Rev. Lett.* **102**, 238102 (2009). https://doi.org/10.1103/PhysRevLett.102.238102

24. Olsson, M. H. M., Søndergaard, C. R., Rostkowski, M. & Jensen, J. H. PROPKA3: consistent treatment of internal and surface residues in empirical pKa predictions. *J. Chem. Theory Comput.* **7**, 525–537 (2011). https://doi.org/10.1021/ct100578z

25. Šali, A. & Blundell, T. L. Comparative protein modelling by satisfaction of spatial restraints. *J. Mol. Biol.* **234**, 779–815 (1993). https://doi.org/10.1006/jmbi.1993.1626

26. Ropp, P. J., Kaminsky, J. C., Yablonski, S. & Durrant, J. D. Dimorphite-DL: an open-source program for enumerating the ionization states of drug-like small molecules. *J. Cheminform.* **11**, 14 (2019). https://doi.org/10.1186/s13321-019-0336-9

27. Bannwarth, C., Ehlert, S. & Grimme, S. GFN2-xTB—An accurate and broadly parametrized self-consistent tight-binding quantum chemical method with multipole electrostatics and density-dependent dispersion contributions. *J. Chem. Theory Comput.* **15**, 1652–1671 (2019). https://doi.org/10.1021/acs.jctc.8b01176

28. Pracht, P., Bohle, F. & Grimme, S. Automated exploration of the low-energy chemical space with fast quantum chemical methods. *Phys. Chem. Chem. Phys.* **22**, 7169–7192 (2020). https://doi.org/10.1039/C9CP06869D

29. Neese, F. Software update: the ORCA program system—version 6.0. *WIREs Comput. Mol. Sci.* **15**, e70019 (2025). https://doi.org/10.1002/wcms.70019

30. Wang, J., Wolf, R. M., Caldwell, J. W., Kollman, P. A. & Case, D. A. Development and testing of a general Amber force field. *J. Comput. Chem.* **25**, 1157–1174 (2004). https://doi.org/10.1002/jcc.20035

31. Morris, G. M. et al. AutoDock4 and AutoDockTools4: Automated docking with selective receptor flexibility. *J. Comput. Chem.* **30**, 2785–2791 (2009). https://doi.org/10.1002/jcc.21256

32. Santos-Martins, D. et al. Accelerating AutoDock4 with GPUs and gradient-based local search. *J. Chem. Theory Comput.* **17**, 1060–1073 (2021). https://doi.org/10.1021/acs.jctc.0c01006

33. Abraham, M. J. et al. GROMACS: high performance molecular simulations through multi-level parallelism from laptops to supercomputers. *SoftwareX* **1–2**, 19–25 (2015). https://doi.org/10.1016/j.softx.2015.06.001

34. Lindorff-Larsen, K. et al. Improved side-chain torsion potentials for the Amber ff99SB protein force field. *Proteins* **78**, 1950–1958 (2010). https://doi.org/10.1002/prot.22711

35. Bouysset, C. & Fiorucci, S. ProLIF: a library to encode molecular interactions as fingerprints. *J. Cheminform.* **13**, 72 (2021). https://doi.org/10.1186/s13321-021-00548-6

36. Valdés-Tresanco, M. S., Valdés-Tresanco, M. E., Valiente, P. A. & Moreno, E. gmx_MMPBSA: a new tool to perform end-state free energy calculations with GROMACS. *J. Chem. Theory Comput.* **17**, 6281–6291 (2021). https://doi.org/10.1021/acs.jctc.1c00645

Funding

This work was supported by the Provincial Secretariat for Higher Education and Scientific Research, Autonomous Province of Vojvodina (Project No. 003864121 2025 09418 003 000 000 001) and by the Ministry of Science, Technological Development, and Innovation of the Republic of Serbia. (The grant agreement with the University of Belgrade, Institute for the Application of Nuclear Energy INEP: 451-03-136/2026-03/200019.) This paper aligns with Agenda 2030 (United Nations Sustainable Development Goal 3), promoting good health and well-being.

Author contributions

L.V. performed the molecular docking and molecular dynamics simulations, analysed the computational data and wrote the original manuscript. J.B. and A.R. contributed to data analysis, interpretation of the findings and manuscript writing and editing. D.D. contributed to the pharmacological rationale of the study and critically evaluated the interpretation of the results. Lj.T. and A.M. reviewed the relevant literature and contributed to placing the findings in the context of previous studies on maslinic and oleanolic acids. Đ.B. contributed to the organisation and presentation of the results and checked the consistency between the manuscript text, tables and figures. A.J. contributed to the interpretation of the ligand–target interactions and their relevance to glucose and lipid metabolism. A.P. contributed to the assessment of the biological

implications and study limitations and to the revision of the Discussion. All authors critically reviewed the manuscript for important intellectual content and approved the final version.

Data availability

The docking and molecular dynamics data are deposited in Zenodo at https://zenodo.org/records/23891971. The deposit includes prepared structures and topologies, docking inputs and outputs, simulation parameters and logs, 48 analysis trajectories at 100 ps intervals, structural and interaction results, and PCA bases, projections and graphs. The deposited directories and files are described in Supplementary Table S15.

Competing interests

The authors declare no competing interests.

Tables and figures

Table 1. Selected docking poses used to initialize molecular dynamics.

Target	Reference (rank)	Reference score	MAS score	OLE score	Reference RMSD (Å)
FXR	CIL (1)	-13.30	-12.10	-12.41	1.602
HSD11B1	CBO (6)	-13.53	-12.13	-12.20	1.154
PPARα	REW (10)	-10.99	-9.21	-10.50	1.065
PTP1B	UN5 (1)	-14.30	-8.22	-7.85	0.865

Scores are in kcal mol^{-1} and are empirical docking scores. Reference RMSD is the ordered heavy-atom deviation of the selected prepared reference ligand from crystal coordinates without ligand superposition. HSD11B1, 11β-hydroxysteroid dehydrogenase type 1; PTP1B, protein tyrosine phosphatase 1B; PPARα, peroxisome proliferator-activated receptor α; FXR, farnesoid X receptor; CIL, cilofexor; CBO, carbenoxolone; PDB, Protein Data Bank; REW, PDB identifier for the co-crystallized PPARα ligand BMS-631707; UN5, PDB component code for the co-crystallized sulfamic-acid PTP1B inhibitor; MAS, maslinic acid; OLE, oleanolic acid. Ranks in parentheses are the original global docking-score ranks in the prepared-reference campaigns (rank 1 denotes the lowest score). CBO and REW were selected for their closer agreement with the crystallographic poses. Selected-versus-top-ranked scores and root-mean-square deviations (RMSDs) are reported in Supplementary Table S2e. The PTP1B candidates occupy proximal site B, while UN5 also spans the catalytic region. Detailed search IDs, clusters, and separate native-redocking results are given in Supplementary Tables S2a, S2b, and S2d.

Table 2. Ligand displacement, protein hydrogen bonds, and MM/PBSA endpoint scores.

Target	Ligand	Ligand RMSD (nm)	Protein H bonds	MM/PBSA score (kcal mol^{-1})
FXR	CIL	0.217 ± 0.014	4.20 ± 0.97	-69.36 ± 3.68
FXR	MAS	0.210 ± 0.042	2.56 ± 0.80	-57.62 ± 0.36
FXR	OLE	0.192 ± 0.013	1.42 ± 0.24	-56.65 ± 1.13
HSD11B1	CBO	0.230 ± 0.018	2.56 ± 0.74	-61.23 ± 3.08
HSD11B1	MAS	0.237 ± 0.166	3.25 ± 0.98	-54.96 ± 2.96
HSD11B1	OLE	0.247 ± 0.056	0.04 ± 0.06	-48.76 ± 0.90
PPARα	REW	0.226 ± 0.076	2.83 ± 0.53	-72.25 ± 2.96
PPARα	MAS	0.307 ± 0.167	1.48 ± 0.48	-53.73 ± 2.44
PPARα	OLE	0.363 ± 0.168	2.16 ± 1.27	-52.87 ± 2.62
PTP1B	UN5	0.191 ± 0.009	9.12 ± 0.36	-52.59 ± 0.17
PTP1B	MAS	0.280 ± 0.013	2.85 ± 0.40	-31.73 ± 0.93
PTP1B	OLE	0.305 ± 0.016	2.18 ± 0.21	-32.13 ± 1.66

Values are the mean ± sample standard deviation of three independently seeded 100 ns trajectory means (n = 3), over 0–100 ns. Ligand root-mean-square deviation (RMSD) follows protein fitting and uses each run's minimized reference. HSD11B1, 11β-hydroxysteroid dehydrogenase type 1; PTP1B, protein tyrosine phosphatase 1B; PPARα, peroxisome proliferator-activated receptor α; FXR, farnesoid X receptor; CIL, cilofexor; CBO, carbenoxolone; PDB, Protein Data Bank; REW, PDB identifier for the co-crystallized PPARα ligand BMS-631707; UN5, PDB component code for the co-crystallized sulfamic-acid PTP1B inhibitor; MAS, maslinic acid; OLE, oleanolic acid; MM/PBSA, molecular mechanics/Poisson–Boltzmann surface area. Hydrogen bonds are mean geometric counts, not contact occupancies. Oxidised nicotinamide adenine dinucleotide phosphate ($NADP^+$; PDB residue code NAP) is excluded from the HSD11B1 protein hydrogen-bond group but included in its MM/PBSA receptor. Endpoint scores comprise molecular-mechanics and solvation contributions and are not calibrated binding free energies. Individual results and alternative time windows are provided in Supplementary Tables S4b, S5b, S6b, S7b, and S8a–d.

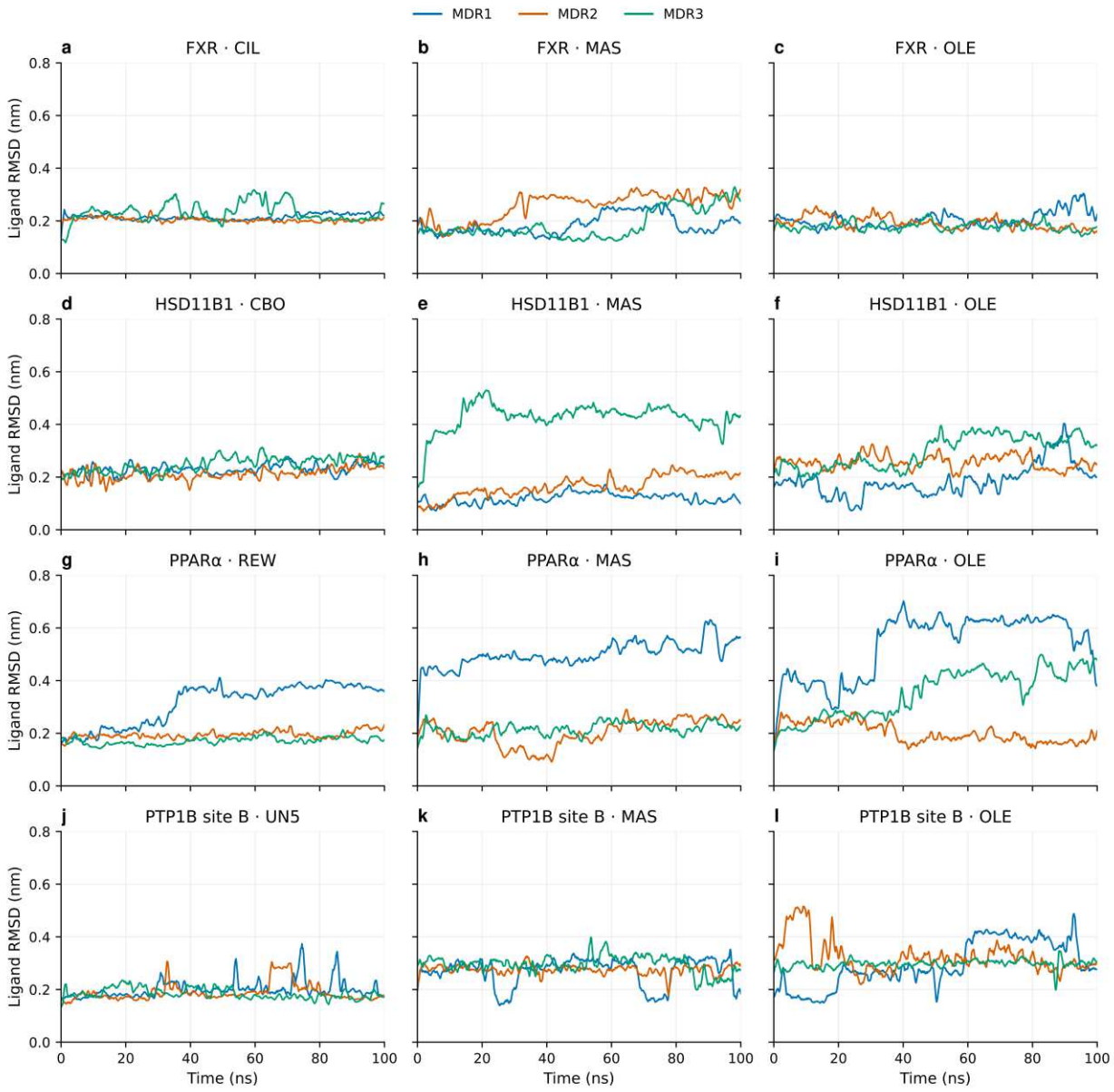


Figure 1. Ligand heavy-atom root-mean-square deviation (RMSD) across the triplicate simulations. Panels show the reference ligand, MAS, and OLE for FXR (a–c), HSD11B1 (d–f), PPARα (g–i), and PTP1B site B (j–l). HSD11B1, 11β-hydroxysteroid dehydrogenase type 1; PTP1B, protein tyrosine phosphatase 1B; PPARα, peroxisome proliferator-activated receptor α; FXR, farnesoid X receptor; CIL, cilofexor; CBO, carbenoxolone; PDB, Protein Data Bank; REW, PDB identifier for the co-crystallized PPARα ligand BMS-631707; UN5, PDB component code for the co-crystallized sulfamic-acid PTP1B inhibitor; MAS, maslinic acid; OLE, oleanolic acid. Blue, orange, and green traces correspond to runs 1 (MDR1), 2 (MDR2), and 3 (MDR3), respectively. Ligand heavy-atom RMSD was calculated relative to each run's minimized structure after least-squares fitting of the protein, without ligand self-fitting. For display, the original 10 ps values were smoothed with a centred 100-frame rolling mean (approximately 1 ns) and plotted every tenth value (0.1 ns), using the reduced window available at trajectory ends. Numerical summaries use the unsmoothed series. All three trajectories within a ligand–target pair began from the same selected docking pose and differed in their initial velocity seed.

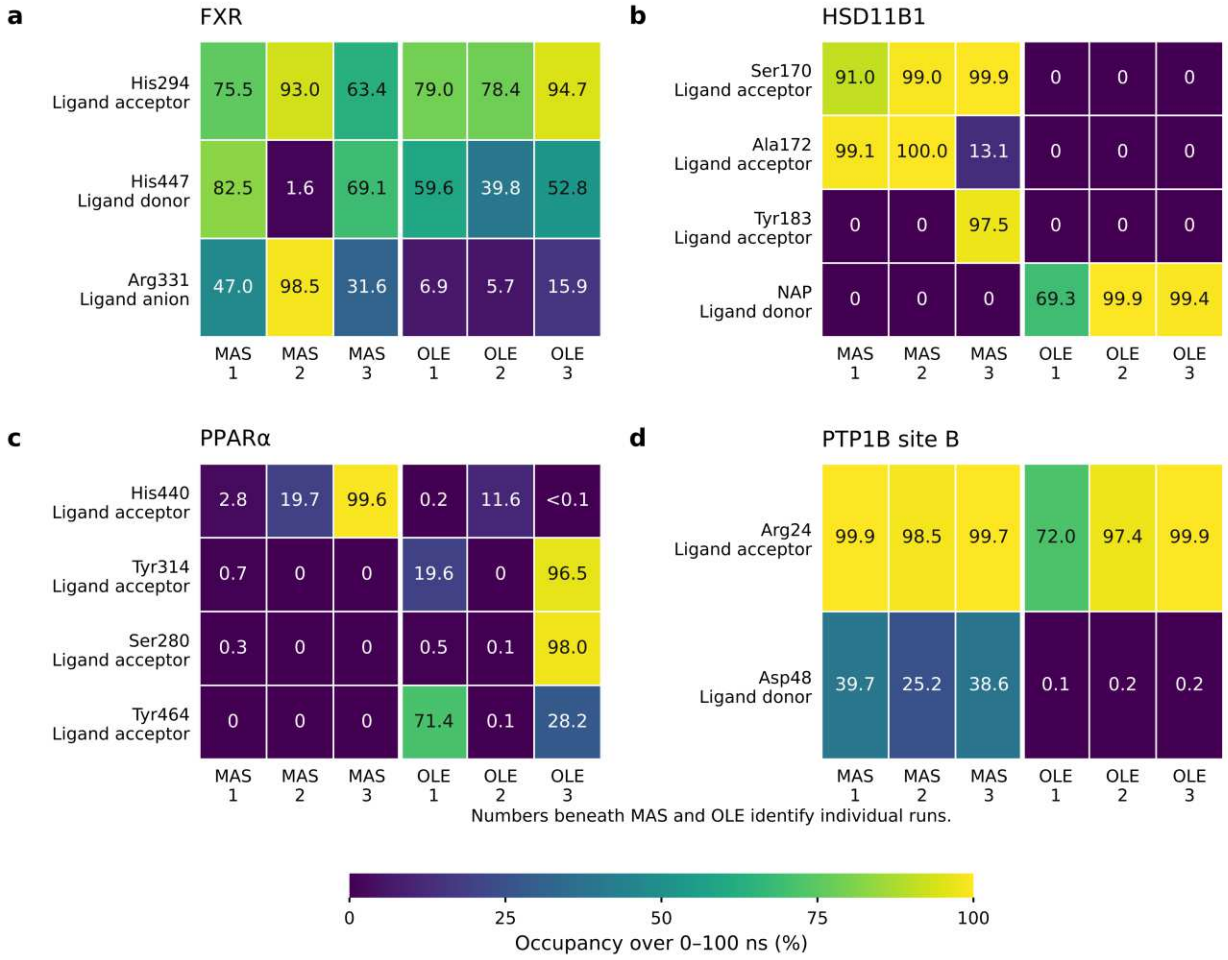


Figure 2. Replica-resolved occupancies of selected polar interactions. ProLIF interaction occupancies over 0–100 ns are shown for MAS and OLE with FXR (a), HSD11B1 (b), PPARα (c), and PTP1B site B (d). HSD11B1, 11β-hydroxysteroid dehydrogenase type 1; PTP1B, protein tyrosine phosphatase 1B; PPARα, peroxisome proliferator-activated receptor α; FXR, farnesoid X receptor; MAS, maslinic acid; OLE, oleanolic acid. Columns represent the three independently seeded trajectories for each ligand. Values are percentages of 10,001 analysed frames, rounded to one decimal place; nonzero values below 0.05% are labelled <0.1. The row labels specify the ligand's role: acceptor and donor correspond to HBAcceptor and HBDonor, while anion corresponds to Anionic. NAP is the Protein Data Bank residue code for the HSD11B1 cofactor, oxidised nicotinamide adenine dinucleotide phosphate ($NADP^+$). Interactions were selected after analysis to illustrate contacts discussed in the text. Zero denotes no detected event under the applied definitions.

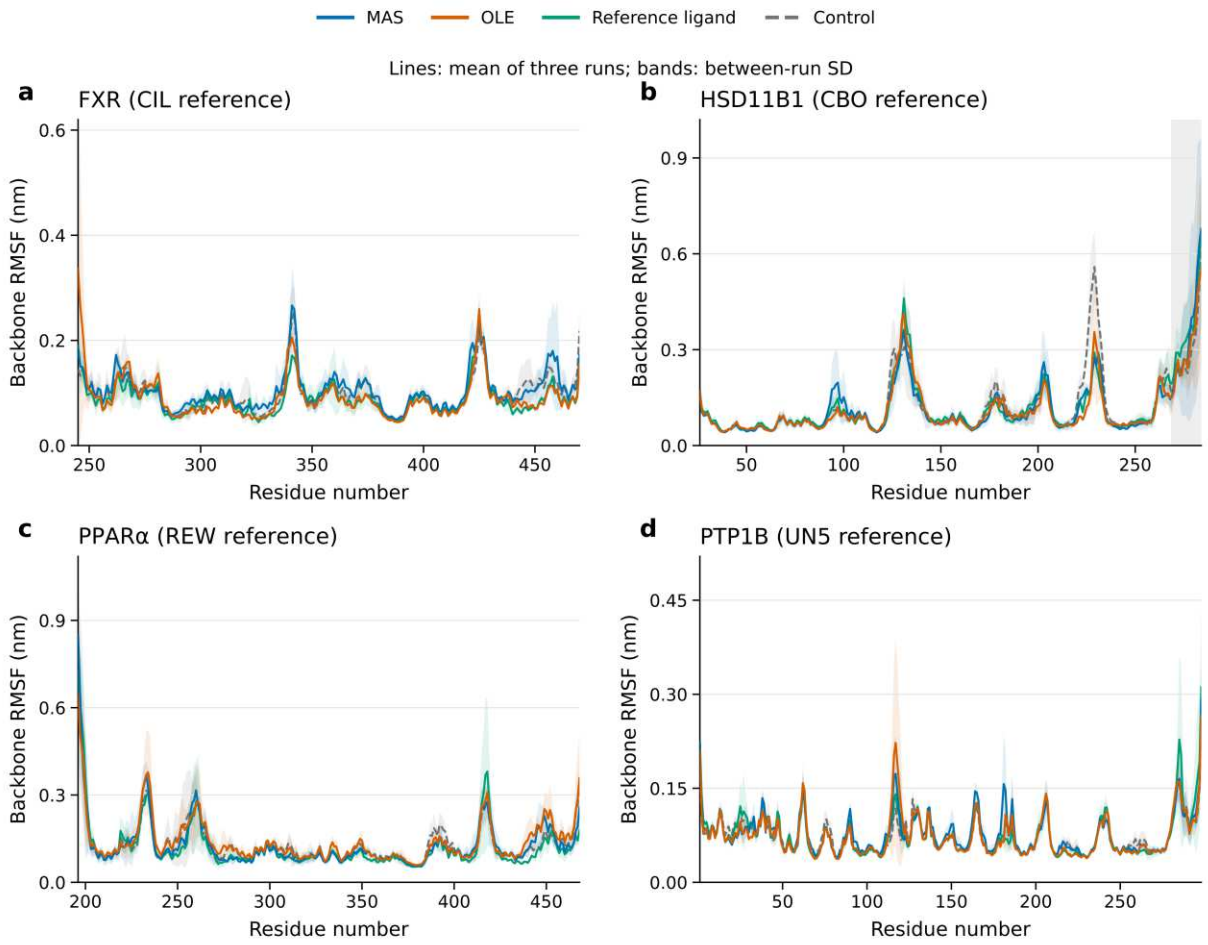


Figure 3. Residue-resolved backbone fluctuations in the triplicate simulations. Backbone root-mean-square fluctuation (RMSF) is plotted using original residue numbering for FXR (a), HSD11B1 (b), PPARα (c), and PTP1B (d). HSD11B1, 11β-hydroxysteroid dehydrogenase type 1; PTP1B, protein tyrosine phosphatase 1B; PPARα, peroxisome proliferator-activated receptor α; FXR, farnesoid X receptor; CIL, cilofexor; CBO, carbenoxolone; PDB, Protein Data Bank; REW, PDB identifier for the co-crystallized PPARα ligand BMS-631707; UN5, PDB component code for the co-crystallized sulfamic-acid PTP1B inhibitor; MAS, maslinic acid; OLE, oleanolic acid. Lines show the arithmetic mean of the three run-specific per-residue RMSF profiles; shaded bands show their sample standard deviation. Each trajectory covers 0–100 ns and uses a different initial velocity seed. Reference ligands are CIL, CBO, REW, and UN5 for the respective targets. Control HSD11B1 retains oxidised nicotinamide adenine dinucleotide phosphate ($NADP^+$; PDB residue code NAP). The grey strip in panel b marks modelled C-terminal residues 269–284. No smoothing was applied. Ordinate ranges differ between targets. Individual trajectories are shown in Supplementary Fig. S4.

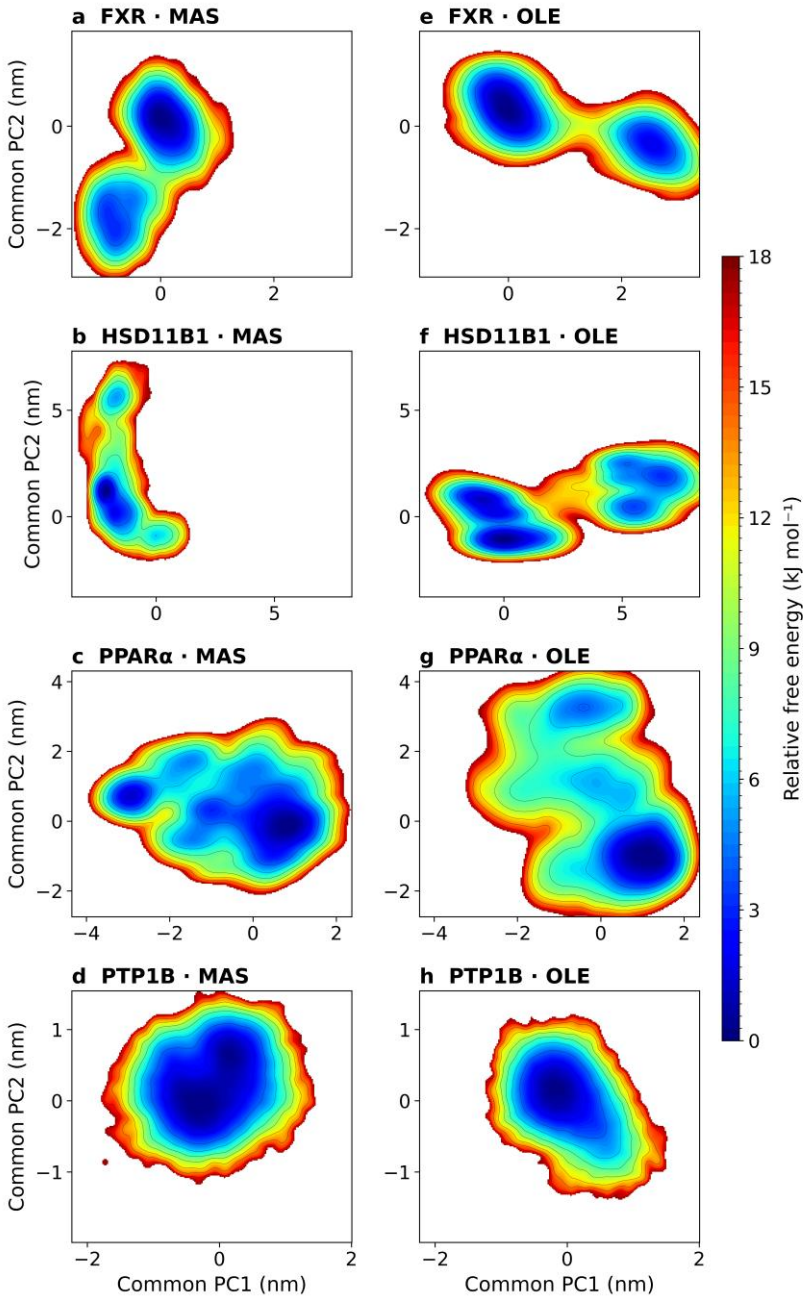


Figure 4. KDE-based projected PC1–PC2 landscapes for MAS and OLE. Panels a–d show MAS and panels e–h show OLE for FXR, HSD11B1, PPARα, and PTP1B, respectively. HSD11B1, 11β-hydroxysteroid dehydrogenase type 1; PTP1B, protein tyrosine phosphatase 1B; PPARα, peroxisome proliferator-activated receptor α; FXR, farnesoid X receptor; MAS, maslinic acid; OLE, oleanolic acid; KDE, kernel density estimation; PC1 and PC2, first and second principal components; Cα, alpha-carbon atoms; R, molar gas constant; T, temperature; ρ, estimated probability density; ρ_{max}, maximum evaluated density. Each receptor uses one shared Cα basis and common coordinate limits. Three replica densities over 0–100 ns were averaged with equal weights before calculating $-RT \ln(\rho/\rho_{max})$ at 310.15 K. Each map has its own zero. The 200 × 200 evaluation mesh and condition-specific diagonal Scott bandwidths produce 64 filled contour bands over 0–18 kJ mol^{-1}, with black contours every 2 kJ mol^{-1}. White regions exceed the display range or have numerically underflowed density. PC1 + PC2 explain 24.91%, 43.43%, 26.44%, and 17.37% of the full covariance variance, respectively. Modelled HSD11B1 residues 269–284 contribute 63.24% and 70.25% of the squared PC1 and PC2 mode norms, respectively. All pooled conditions and individual replicas appear in Supplementary Figs. S5–S9; bandwidths are listed in Supplementary Table S13d.

Supplementary Files

This is a list of supplementary files associated with this preprint. Click to download.

- SCIREPsupplementaryLukaVidovic.docx